Mechanisms for Fracture and Fatigue-Crack Propagation in a Bulk Metallic Glass

C.J. GILBERT, V. SCHROEDER, and R.O. RITCHIE

The fracture and fatigue properties of a newly developed bulk metallic glass alloy, $Zr_{41.2}Ti_{13.8}Cu_{12.5}Ni_{10}Be_{22.5}$ (at. pct), have been examined. Experimental measurements using conventional fatigue precracked compact-tension C(T) specimens (~7-mm thick) indicated that the fully amorphous alloy has a plane-strain fracture toughness comparable to polycrystalline aluminum alloys. However, significant variability was observed and possible sources are identified. The fracture surfaces exhibited a vein morphology typical of metallic glasses, and, in some cases, evidence for local melting was observed. Attempts were made to rationalize the fracture toughness in terms of a previously developed micromechanical model based on the Taylor instability, as well as on the observation of extensive crack branching and deflection. Upon partial or complete crystallization, however, the alloy was severely embrittled, with toughnesses dropping to ~1 MPa$\sqrt{m}$. Commensurate with this drop in toughness was a marginal increase in hardness and a reduction in ductility (as measured *via* depth-sensing indentation experiments). Under cyclic loading, crack-propagation behavior in the amorphous structure was similar to that observed in polycrystalline steel and aluminum alloys. Moreover, the crack-advance mechanism was associated with alternating blunting and resharpening of the crack tip. This was evidenced by striations on fatigue fracture surfaces. Conversely, the (unnotched) stress/life (S/N) properties were markedly different. Crack initiation and subsequent growth occurred quite readily, due to the lack of microstructural barriers that would normally provide local crack-arrest points. This resulted in a low fatigue limit of ~4 pct of ultimate tensile strength.

I. INTRODUCTION

FIRST developed some 40 years ago,[1] amorphous metallic alloys have long represented an intriguing class of potential structural materials. The lack of any long-range order and the subsequent absence of microstructure has led to a range of interesting properties. These include near-theoretical strength, large elastic deflections, high hardness, excellent wear properties, and good potential for forming and shaping. Due to the very high cooling rates ($>10^5$ K/s) necessary to prevent crystallization, however, all prior attempts to characterize the mechanical properties have been confined to very thin ribbons or wires (~10 to 100 μm). Indeed, past studies have focused almost exclusively on constitutive properties, as the restrictive nature of the ribbons made the measurement of fracture and fatigue properties very difficult.

Early studies established that, unlike oxide glasses, metallic glasses can be quite ductile.[2–5] Flow in metallic glass is often inhomogeneous, particularly at high stresses and low temperatures, localizing into slip bands along planes of maximum shear. Although the precise flow mechanisms are unclear, bubble-raft and computational studies suggest that they are associated with localized atomic-shear rearrangements correlated to regions of either excess free volume[4,6,7] or extreme shear-stress concentration.[8] Such flow mechanisms, however, have never been verified experimentally due to both a lack of data and the difficulty in characterizing the internal state at the atomic level.

C.J. GILBERT, Postdoctoral Research Associate, V. SCHROEDER, Graduate Student Research Assistant, and R.O. RITCHIE, Professor, are with the Department of Materials Science and Mineral Engineering, University of California, Berkeley, CA 94720-1760.

Manuscript submitted March 25, 1998.

Even less work has been completed on fracture toughness and fatigue-crack propagation in amorphous metals, aside from early limited studies on thin ribbons.[7,9–19] Moreover, since traditional notions of microstructure, crystal defects, and dislocation plasticity (which govern our understanding of the behavior of crystalline alloys) do not apply, the mechanisms and microstructural parameters which govern fracture toughness and fatigue-crack propagation in metallic glasses are essentially unknown.

The recent development of bulk metallic glass permits, for the first time, detailed measurement of fatigue and fracture characteristics, as the severe specimen-geometry limitations associated with rapid quenching no longer apply. In recent years, several families of multicomponent metallic alloys have been developed which exhibit exceptional glass-forming ability. These include, for example, Mg-based alloys like Mg-Cu-Y,[20] some recently discovered Fe-based alloys,[21] and the Zr-Ti-Ni-Cu, Zr-Ti-Ni-Cu-Be, and Zr-Ti-Ni-Cu-Al alloys.[22,23] All exhibit very high resistance to crystallization in the undercooled liquid state, so that relatively low cooling rates result in a fully amorphous structure (typically <10 K/s). For example, the first commercial alloy of $Zr_{41.2}Ti_{13.8}Cu_{12.5}Ni_{10}Be_{22.5}$ (at. pct), also known by its trade name VITRELOY,* requires cooling rates of only ~1 K/s. Thus, fully amorphous rods several centimeters in diameter have been produced.[22] Because of its high strength-to-stiffness ratio and low damping characteristics, $Zr_{41.2}Ti_{13.8}Cu_{12.5}Ni_{10}Be_{22.5}$ is now being used to fabricate golf-club heads.

*Vitreloy is a trademark of Amorphous Technologies International, Corp.

Although preliminary studies indicate that $Zr_{41.2}Ti_{13.8}Cu_{12.5}Ni_{10}Be_{22.5}$ and some related alloys exhibit high fracture toughness, along with fatigue-crack growth properties comparable to those of high-strength steel and aluminum

Table I. Elemental Composition in Mass Fraction Weight Percent*

Sample	Zr	Ti	Cu	Ni	Be	O	N
1	62.60	10.92	12.90	10.00	3.730	0.1011	0.0043
2	62.40	10.87	12.84	10.20	3.800	0.1076	0.0056

*Courtesy Howmet Research Corporation (Whitehall, MI).

alloys,[24–28] these results are not understood mechanistically. In addition, recent work has demonstrated that, upon partial or full crystallization, the alloy is severely embrittled[24] (similar to a number of other amorphous alloys).[11,17,29] Accordingly, the objective of the current study is to quantify the fracture toughness and fatigue-crack growth properties of this bulk metallic glass alloy in further detail and to develop a mechanistic understanding of fracture and fatigue in this class of materials.

II. EXPERIMENTAL PROCEDURES

A. *Material and Microstructure*

Experiments were performed on as-cast plates (7-mm thick, 40 × 40 mm) of fully amorphous $Zr_{41.2}Ti_{13.8}Cu_{12.5}Ni_{10}Be_{22.5}$ in at. pct ($Zr_{62.6}Ti_{11.0}Cu_{13.2}Ni_{9.80}Be_{3.40}$ in wt pct). Castings were produced by Hitchener Manufacturing Co. (Milford, NH) and were supplied by Amorphous Technologies International (Laguna Niguel, CA). This alloy was originally developed by Peker and Johnson, and processing methods are described elsewhere.[22] The chemistries of two separate batches are shown in Table I (measured using mass spectroscopy). Notice that significant amounts of oxygen and nitrogen are present in both heats. These oxygen levels (~3700 ppm) are substantially higher than those reported by Conner *et al.* (800 ppm)[26] or by Lowhaphandu *et al.* (1600 ppm).[28] Typical mechanical and thermal properties are listed in Table II.[22,24,30,31]

As-received plates were found to be fully amorphous, as indicated by transmission electron microscopy studies (Figure 1).[32] By heat treating specimens in vacuum (~10^{-6} torr) at 633 K, for times ranging from 0.1 to 24 hours, several partially crystallized structures were formed. The specimen heat treated at 633 K for 12 hours, for example, consisted of an amorphous matrix containing ~3- to 5-nm-long crystallites of a Cu-rich, Ti-rich fcc phase, with an average spacing of ~20 nm between nanocrystals (Figure 2).[32] The volume fraction of the crystalline fcc phase was estimated from X-ray and transmission electron microscopy data to be less than 5 pct of the sample.[33,34,35] By heat treating at 723 K for 24 hours in vacuum, a fully crystallized multiphase microstructure was obtained, containing a Laves phase with the hcp "$MgZn_2$-type" structure,[34] a phase with the "Al_2Cu-type" structure, and at least one additional unidentified phase.[33,36,37] The X-ray diffraction patterns (Cu K_α) corresponding to each of the heat treatments examined are shown in Figure 3 and indicate the transition from a fully amorphous to a fully crystallized microstructure after annealing for 24 hours at 723 K.

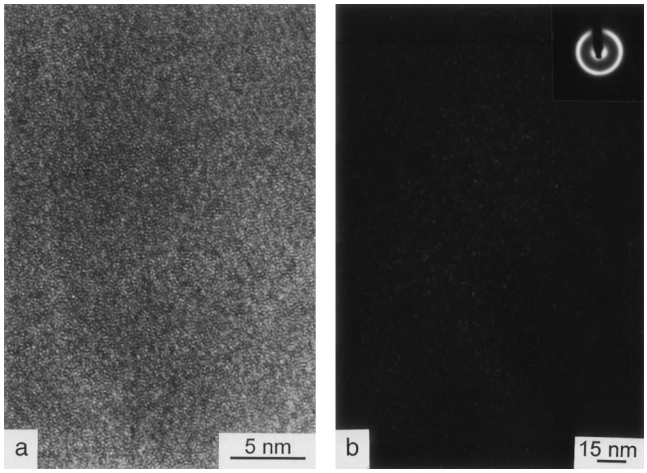

Fig. 1—High-resolution transmission electron microscopy, in (*a*) bright field and (*b*) dark field, of the as-received, fully amorphous $Zr_{41.2}Ti_{13.8}Cu_{12.5}Ni_{10}Be_{22.5}$ alloy (courtesy of W.L. Johnson).[32]

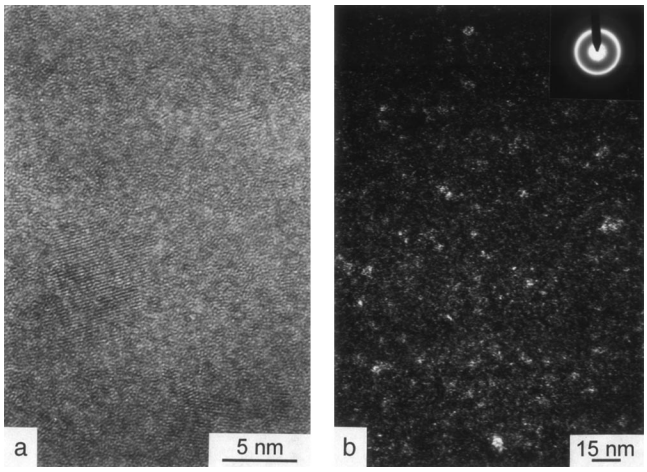

Fig. 2—High-resolution transmission electron microscopy, in (*a*) bright field and (*b*) dark field, of the $Zr_{41.2}Ti_{13.8}Cu_{12.5}Ni_{10}Be_{22.5}$ alloy annealed at 633 K for 12 h (courtesy of W.L. Johnson).[32] Notice the appearance of lattice fringes not visible in the as-received structure.

Table II. Selected Properties of $Zr_{41.2}Ti_{13.8}Cu_{12.5}Ni_{10}Be_{22.5}$ Bulk Metallic Glass

Density (g/cm^3)	Young's Modulus (GPa)	Shear Modulus (GPa)	Poisson's Ratio	Yield Strength (GPa)	Vickers Hardness (GPa)	Glass Transition† (K)	Fracture Toughness* (MPa$\sqrt{m}$)
5.9	95	35	0.35	1.9	5.4	~625	~55

*Measured at a K of 0.3 MPa$\sqrt{m}$ s^{-1} on a 7-mm-thick, fatigue-precracked compact tension sample.[24]
†Measured at a scan rate of 0.33 K/s.[22]

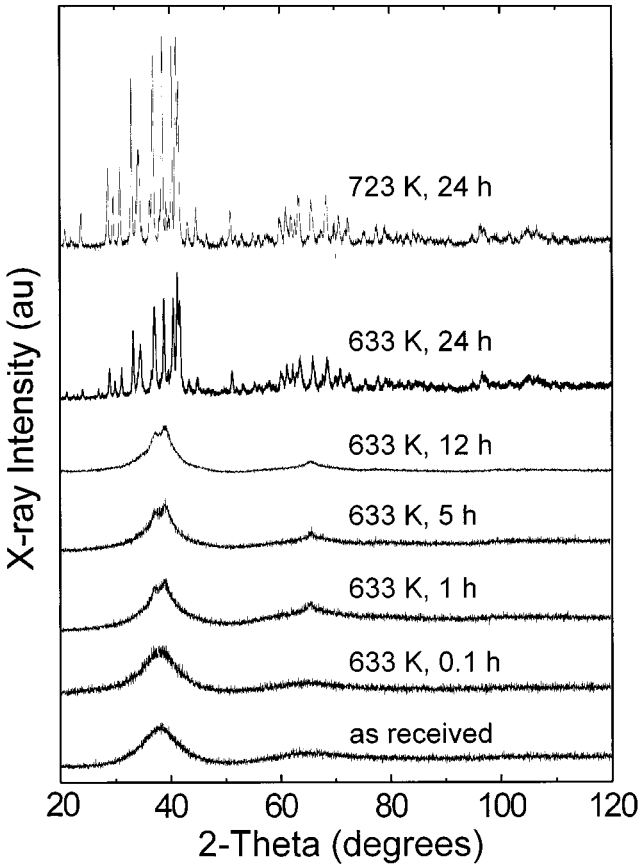

Fig. 3—X-ray diffraction patterns corresponding to each of the annealing conditions examined in this study, indicating the transition from the fully amorphous, as-received alloy to the fully crystallized alloy after 24 h at 723 K.

B. *Hardness and Contact-Damage Measurements*

The Vickers hardness (H) was determined by indenting specimens polished to a ~1 μm finish (Acroscope, Santa Clara, CA) at a load of 49 N, with measurements averaged over at least 5 indents. This indentation load was selected in order to minimize chipping when testing the partially and fully crystallized specimens. In addition, depth-sensing indentation experiments with hardened stainless steel spherical indenters (radius (r) of 3.18 mm) were used to obtain single loading-unloading hysteresis curves for a fully amorphous, partially crystallized (633 K for 12 hours) and a fully crystallized (723 K for 24 hours) microstructure. Measurements were performed on a servohydraulic mechanical test frame operating in load control, using a swing-arm displacement gage resting on the specimen surface for depth sensing.

C. *Fatigue-Crack Growth Rate Measurements*

Fracture toughness and fatigue-crack growth rates were determined in a room-air environment (22 °C, ~45 pct relative humidity) on 7-mm-thick, 38-mm-wide compact-tension C(T) specimens. Samples were cut from the as-received plates using electrodischarge machining. For these specimens, the thickness was not changed significantly from the original castings, and only one face was polished prior to testing. Polished surfaces were prepared using standard lapping techniques with minimal surface removal (<50 μm). Limited testing was also performed on thinned C(T) samples, due to concern about surface residual stress. In these samples, ~1.5 mm was removed from *each* surface prior to testing, again using electrodischarge machining. This reduced the sample thickness from 7 to 4 mm.

Specimens were cycled under stress-intensity (K) control, with a test frequency (ν) of 25 Hz (sinusoidal waveform), under constant-load-ratio (R) conditions. Testing was performed on computer-controlled, servohydraulic mechanical testing machines, in general accordance with ASTM standard E647. The load ratio, defined as the ratio of minimum to maximum load in the loading cycle (for tensile loading, equivalent to K_{min}/K_{max}), was varied from 0.1 to 0.5. To obtain a wide spectrum of growth rates, samples were first cycled with a decreasing stress-intensity range (at normalized K gradients of 0.08 and 0.2 mm^{-1})* until measured growth rates were less than 10^{-10} m/cycle. The value of the stress-intensity range at this point was used to operationally define the fatigue threshold stress intensity (ΔK_{TH}) below which long cracks are essentially dormant. After threshold determination, specimens were cycled under increasing ΔK conditions with the same K gradient, up to growth rates of 10^{-7} m/cycle.

*Although ASTM E647 specifies a maximum load-shedding rate of 0.08 mm^{-1}, faster K gradients of up to 0.20 mm^{-1} were found to give identical results, as is typical of higher-strength materials.

Cracks initiated readily from the as-machined notches, and, so, a half-chevrons notch was not necessary to initiate stable cracking. Samples were fatigue precracked for several millimeters beyond this notch prior to data collection.*

*Some specimens were rejected due to cracks which initiated and grew perpendicular to the machined notch. This was only a problem with 7-mm-thick CT samples and appeared to be associated with residual stress. Sequential cutting techniques,[38] for example, revealed compressive stresses of ~450 MPa at the surface of some castings.[39]

Thereafter, crack lengths were continuously monitored using unloading elastic-compliance measurements, with a 350 Ω strain gage attached to the back face of the specimen. Readings were checked periodically using a traveling microscope. Optical and compliance measurements were always found to be within 2 pct. Data are presented in terms of the growth rate per loading cycle (da/dN) as a function of the alternating stress-intensity range of $K_{max} - K_{min}$, the latter being computed using standard linear-elastic handbook solutions.

Fatigue-crack closure, defined in the metals literature as premature contact of mating crack faces on unloading, was also monitored using a strain gage attached to the back face of the specimen. The closure stress intensity (K_{cl}) was approximately defined at the point where the elastic unloading line initially deviated from linearity on a plot of load (P) *vs* back-face strain (ε). Under plane-strain conditions, crack closure may generally be considered to arise from asperity contact some distance behind the crack tip. This reduces the local stress-intensity range actually experienced at the crack tip to an effective level (ΔK_{eff}) of $K_{max} - K_{cl}$, where $K_{cl} > K_{min}$.

During and after fracture and fatigue experiments, the crack profiles and fracture surfaces of selected specimens

were analyzed with both an optical microscope and in the scanning electron microscope (SEM), with the objective of elucidating the salient mechanisms of fracture and fatigue-crack growth.

D. *Variable-Amplitude Fatigue-Crack Growth Behavior*

Limited studies were also made of transient crack-growth behavior following variable-amplitude loading sequences. For variable-amplitude loading tests, crack-growth rates were measured under constant ΔK conditions, with $R = 0.1$ and $\nu = 25$ Hz. Once a steady-state crack growth rate was achieved, specimens were subjected to a block-loading sequence in order to examine transient crack-growth behavior. Transient data are presented as the growth rate per cycle plotted against crack extension (Δa).

E. *Fracture Toughness Measurements*

Following growth-rate measurements, fracture toughness values in the fully amorphous structure were determined by monotonically loading the fatigue-precracked specimens to failure at specified loading rates (K), in general accordance with ASTM standard E399. However, because fatigue cracking was unstable in the partially and fully crystalline structures due to their extreme brittleness, toughness values were obtained using indentation methods for these microstructures. In each case, measurements were averaged from at least five Vickers hardness indents under an indentation load (P_{ind}) of 49 N. Fracture toughness values (K_{Ic}) were calculated from[40]

$$K_{Ic} = \chi \frac{P_{\text{ind}}}{c^{3/2}} \qquad [1]$$

where the $2c$ is the total surface crack length and χ is a constant dependent upon indent geometry and material properties. For brittle solids, χ can be estimated to be $0.016(E/H)^{1/2}$, where E is the elastic modulus and H is the hardness.[40]

F. *Stress-Life Measurements*

Fatigue lifetimes (N_f) were measured over a range of cyclic stresses by cycling $3 \times 3 \times 50$ mm rectangular beams in four-point bending, with an inner span (S_1) and outer span (S_2) of 10.2 and 20.3 mm, respectively. The specimens, which had been previously polished to an ~ 1 μm surface finish, were cycled under load control at $\nu = 25$ Hz (sinusoidal waveform) with a load ratio of $R = 0.1$ in a room-air environment (25 °C, ~45 pct relative humidity) on a servohydraulic mechanical test frame. Stresses were calculated at the tensile surface within the inner span using the equation

$$\sigma = \frac{3P(S_2 - S_1)}{2bh^2} \qquad [2]$$

where P is the applied load, b is the specimen thickness, and h is the specimen height. A total of 21 beams were tested at maximum stresses ranging from 100 to 1800 MPa (just below the tensile failure stress), with multiple measurements made at each stress when possible. Tests were terminated in cases where failure had not occurred after 2×10^7 cycles (~9 days at 25 Hz). Fracture surfaces of selected beams were examined after failure *via* both optical microscopy and scanning electron microscopy, in order to discern the origin and mechanisms of failure. Stress/life (S/N) data are presented in terms of the stress amplitude (σ_a, equal to 1/2 ($\sigma_{\max} - \sigma_{\min}$), normalized by the uniaxial tensile strength (σ_u, equal to 1.9 GPa[30]), plotted as a function of the number of cycles to failure (N_f), where one cycle is defined as a full stress reversal.

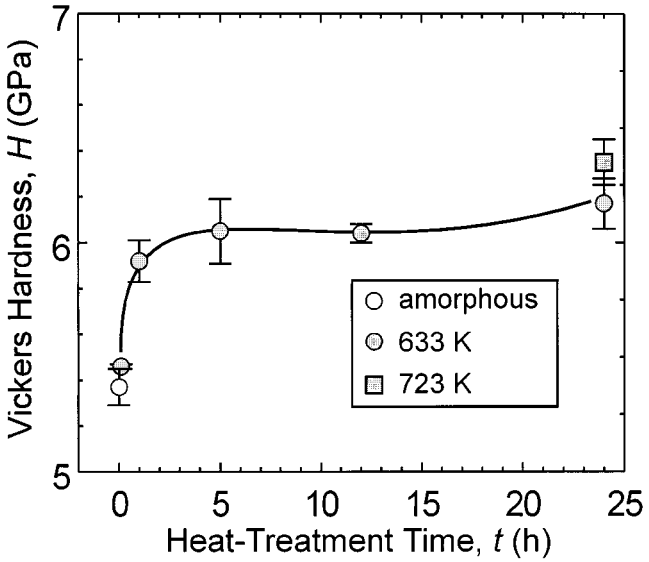

Fig. 4—Vickers hardness, H, plotted as a function of annealing time, t, for specimens heat treated at both 633 and 723 K in vacuum. Data are compared to the as-received, amorphous sample.

III. DEFORMATION AND FRACTURE TOUGHNESS

A. *Hardness and Contact Damage*

The Vickers hardness increased marginally from 5.37 (±0.08) GPa in the amorphous structure to 6.17 (±0.11) and 6.35 (±0.10) GPa in the partially (24 hours at 633 K) and fully (24 hours at 723 K) crystallized structures, respectively. For anneals at 633 K, the majority of the increase in hardness occurred within the first 1 hour of heat treatment (Figure 4), coincident with only a slight sharpening of the X-ray pattern (Figure 3). Other studies of essentially the same alloy ($Zr_{41}Ti_{13}Cu_{13}Ni_{10}Be_{23}$) have reported an even higher hardness (~9.5 GPa) after annealing at 930 K for 2 hours.[36]

A catastrophic shear instability in the fully amorphous structure severely limits the amount of macroscopic plasticity, or stable elongation after the elastic limit, that can be measured with a conventional tensile test.[30] (Note that in compression, however, plastic strains of several percentages are observed.[30]) Because the deformation zone under an indent is more stable, depth-sensing indentation experiments on selected microstructures were used to measure changes in deformation behavior upon crystallization (Figure 5). In the amorphous metal, substantial plastic deformation was observed in the form of hysteresis in the loading-unloading curve and a permanent depression remained on the specimen surface (Figure 5(a)). After heat treating the sample at 633

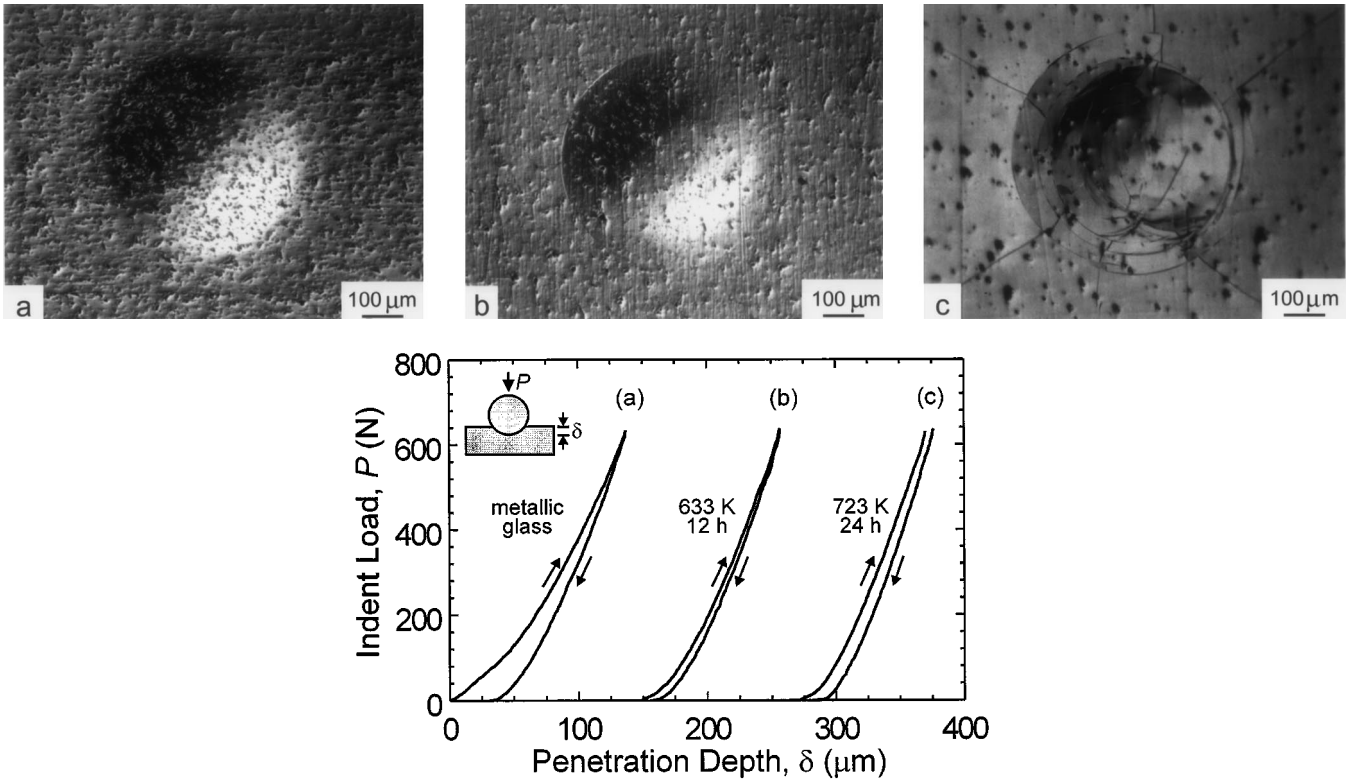

Fig. 5—Depth-sensing indentation measurements and optical micrographs of the remaining hardness impressions of (*a*) a fully amorphous specimen, (*b*) a specimen annealed at 633 K for 12 h, and (*c*) a specimen annealed at 723 K for 24 h.

K for 12 hours (Figures 2 and 3), the degree of hysteresis was markedly reduced, and a Hertzian ring crack formed around the indent (Figure 5(b)). Finally, after 24 hours at 723 K, severe cracking was observed under the indent, and a distinct jump associated with such cracking was recorded at the peak indent load (Figure 5(c)). In this case, the hysteresis was associated primarily with cracking rather than plastic deformation. Consistent with the increase in hardness, the total penetration depth at peak load decreased from ~140 μm in the amorphous structure to ~110 μm in the partially (12 hours at 633 K) crystallized microstructure and to ~100 μm in the full (24 hours at 723 K) crystallized microstructure.

B. *Fracture Toughness*

Both the 7-mm and the 4-mm thick C(T) samples exceeded the plane-strain thickness requirement in ASTM E399, *i.e.*, $B > 2.5(K_{Ic}/\sigma_Y)^2 \sim 2$ mm. Because of crack branching in the 7-mm-thick specimens, however, these fracture toughness values do not strictly conform to ASTM E399; we therefore refer to them as K_Q rather than K_{Ic}. Significant variability was observed in the fracture-toughness data. Sources of this variability may be associated with residual stresses at the surface of castings, compositional variation (particularly oxygen), crack branching and ligament bridging, and sensitivity to loading rate; these issue are discussed more fully subsequently. The highest measured value was ~68 MPa$\sqrt{\text{m}}$ (measured with a 7-mm-thick sample), and the lowest was ~30 MPa$\sqrt{\text{m}}$ (measured with a 4-mm-thick sample). For example, a plot of load *vs* back-face strain is shown in Figure 6 for the 7-mm-thick specimen, which failed at ~68 MPa$\sqrt{\text{m}}$ (K = 0.012 MPa$\sqrt{\text{m}}$ s^{-1}).

Thermal exposure, resulting in partial or full crystallization, led to a dramatic reduction in fracture toughness to ~1 MPa$\sqrt{\text{m}}$ (Figure 7). While the toughness of the amorphous microstructure is comparable to that of a typical polycrystalline aluminum or steel alloy, the toughness after partial or full crystallization is comparable to that of silica

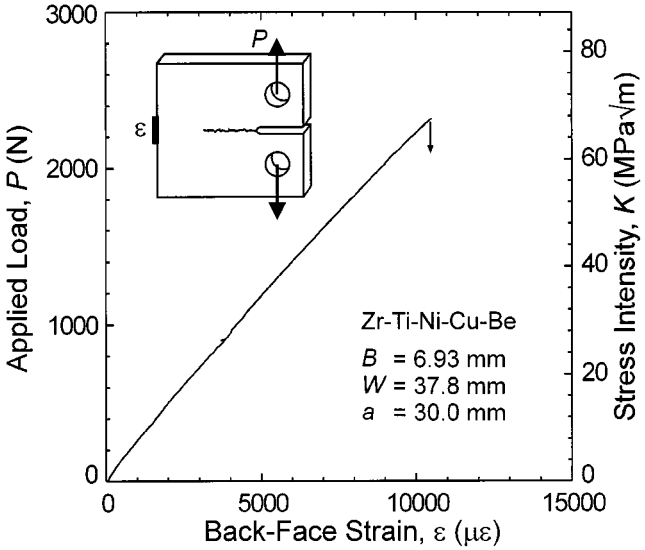

Fig. 6—A typical plot of load, *P, vs* back-face strain, ε, for a specimen loaded to failure. Fracture occurred at $K_Q \sim$ 68 MPa$\sqrt{\text{m}}$ (at a loading rate, K, of 0.012 MPa$\sqrt{\text{m}}$ s^{-1}). Vertical arrow indicates catastrophic failure.

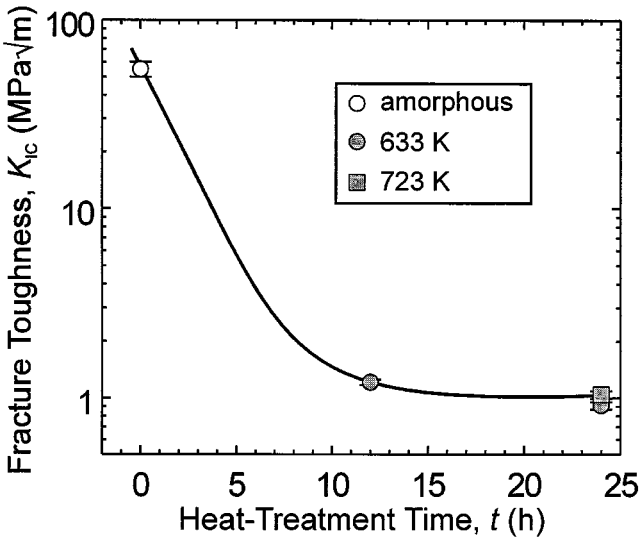

Fig. 7—Fracture toughness plotted as a function of annealing time for specimens heat treated at both 633 and 723 K in vacuum. Data are compared to the as-received, amorphous samples, which were tested at a K of 0.012 to 0.3 MPa$\sqrt{\text{m}}$ s^{-1}.

glass. Similarly, severe embrittlement was observed in a melt-spun ribbon (57 μm thick) of amorphous $Ni_{78}Si_{10}B_{12}$, where the fracture toughness dropped from 67 to 14 MPa$\sqrt{\text{m}}$ after annealing at 713 K for 7 minutes.[17]

Fracture surfaces in the fully amorphous Zr-Ti-Ni-Cu-Be specimens exhibited a veinlike morphology (Figures 8(a) through (c)), typical of many metallic glasses.[3,5] In some regions, these ridges were quite large and ran nominally parallel to the direction of crack propagation (Figures 8(a) and (b)). At higher magnifications, a vein pattern typical of metallic-glass fracture was observed (Figure 8(c)). Stereophotogrammetric investigations of matching fracture surfaces reveal that the tips of the ridges in Figure 8(c) match across the fracture plane[41] and show evidence of substantial local necking and plastic deformation. The features in Figure 8(c) have been likened to that found after the separation of grease or adhesive films.[2,3,42] In some cases, fracture-surface morphologies were strongly suggestive of local melting during fracture (Figure 9). In marked contrast, fracture surfaces in the partially and fully crystallized structures were relatively featureless at comparable magnifications (Figure 8(d)).

IV. FATIGUE-CRACK GROWTH AND STRESS-LIFE BEHAVIOR

A. *Fatigue-Crack Growth Rate Behavior*

The drastic embrittlement upon crystallization meant that stable fatigue cracking was not observed in the annealed

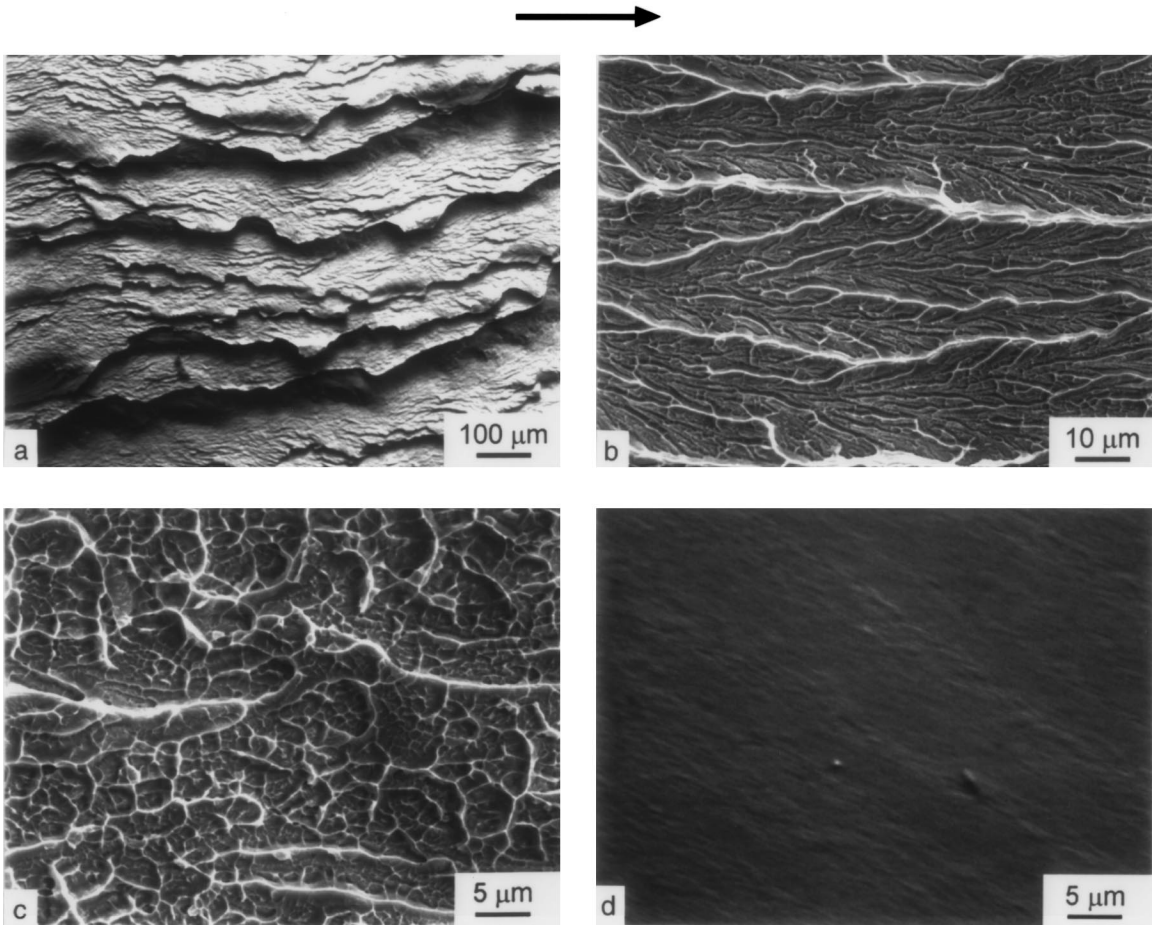

Fig. 8—Scanning electron micrographs at increasing magnification of overload fracture surfaces in (*a*) through (*c*) the fully amorphous alloy and (*d*) a partially crystallized specimen annealed at 633 K for 12 h. The arrow indicates the direction of crack propagation.

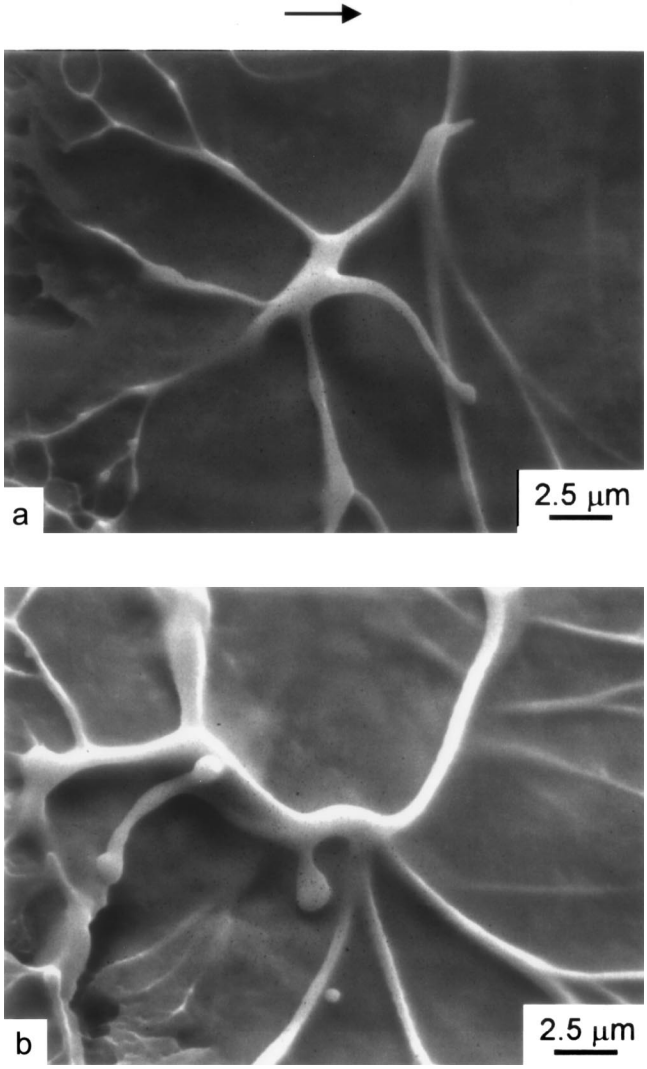

Fig. 9—(*a*) and (*b*) Scanning electron micrographs of an overload fracture surface in the as-received, fully amorphous specimen. These morphologies are strongly suggestive of local melting during fracture. The arrow indicates the direction of crack propagation.

samples (specifically, samples annealed at 633 K for 12 hours and at 723 K for 24 hours). Any attempt to grow stable cracks from the machined notches led to catastrophic failure. Such behavior is typical of very brittle (untoughened) ceramics and is consistent with the precipitous drop in toughness upon crystallization.

In the fully amorphous metal, however, stable fatigue-crack growth was readily characterized under cyclic loading. Growth rates are plotted against ΔK in Figure 10(a), for a specimen tested at $R = 0.1$ and $\nu = 25$ Hz. Unlike most previous results for metallic glasses, these data represent crack growth under plane-strain conditions (Table III). The growth-rate behavior is compared to that of an ultrahigh-strength steel (300-M, quenched, and 200 °C-tempered Si-modified 4340)[43] and an age-hardened aluminum alloy (2090-T81)[44] in Figure 10(b). It is apparent that the cyclic crack growth rates in the amorphous metal are comparable to those observed in traditional polycrystalline metallic alloys. Indeed, when these data are regression fit to a simple Paris power-law equation,[45]

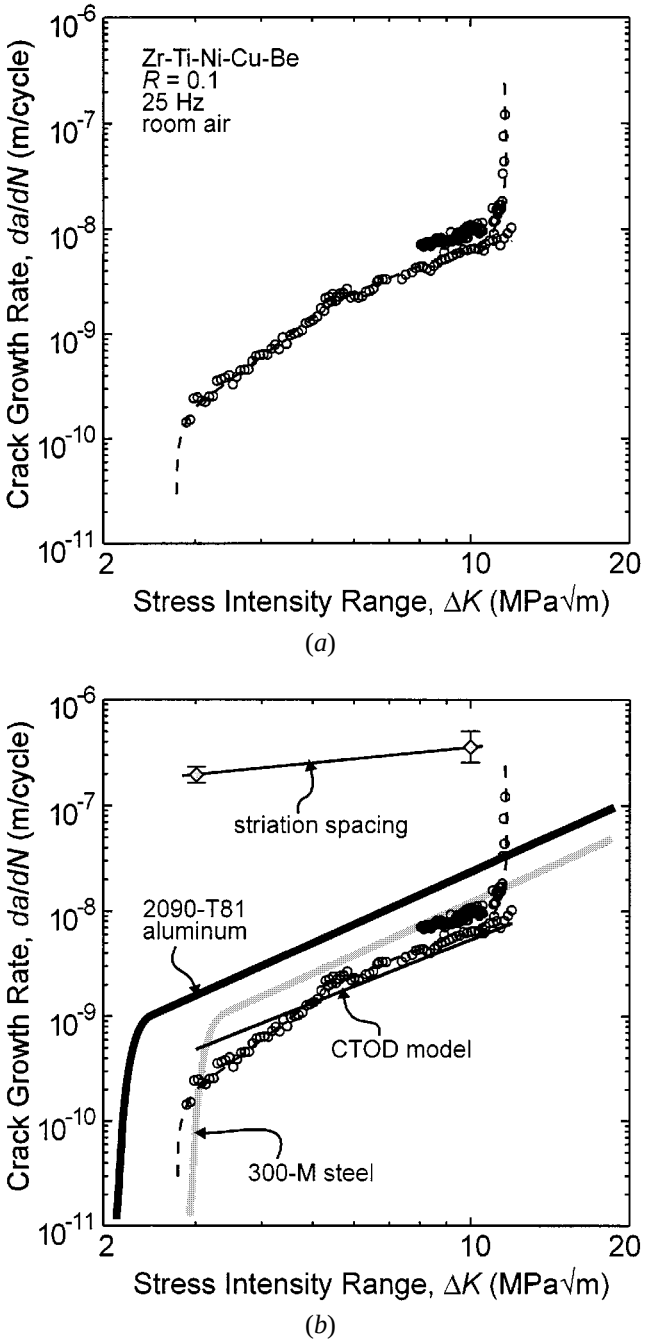

Fig. 10—Results in the form of growth rates, *da*/*dN*, plotted as a function of ΔK (*a*) are shown for a range of fully amorphous specimens ($R = 0.1$ and $\nu = 25$ Hz) and (*b*) are compared with behavior in a high-strength steel (300-M) and an age-hardened aluminum alloy (2090-T81). Also shown in (b) are the striation spacing measurements and prediction from the crack-tip opening displacement model (Eq. [6]).

$$\frac{da}{dN} = C' \Delta K^m \qquad [3]$$

(where m is the crack-growth exponent and C' is a scaling constant), the exponent m in the midrange of growth rates ($\sim 10^{-10}$ to 10^{-7} m/cycle) lies in the range of $m \sim 2$ to 5 (Figure 10 and Table III), typical of ductile crystalline metals in this regime. These values of m are in marked contrast to the fatigue properties of ceramics[46] and oxide glass,[47] where m typically lies in the range of $m \sim 15$ to 50. Values

Table III. Fatigue-Crack Growth Properties of Metallic Glasses (at $R = 0.1$)

Alloy	Reference	Thickness, B (μm)	C' (m/cycle) (MPa$\sqrt{\text{m}})^{-m}$	m	ΔK_{TH} (MPa$\sqrt{\text{m}}$)
$Pd_{80}Si_{20}$	15	~60 to 65	—	4	9
$Ni_{39}Fe_{38}P_{14}B_6Al_3$	9	~43	2.8×10^{-10}	2.25	6
$Fe_{40}Ni_{40}P_{14}B_6$	11	10	5.8×10^{-11}	3.85	2
$Co_{72.15}Fe_{5.85}Mo_2B_{15}Si_5$	16	30	1.2×10^{-11}	3.3	7
$Co_{76.05}Fe_{1.95}Mn_4B_{12}Si_6$	16	30	1.4×10^{-13}	5.7	5
$Ni_{78}Si_{10}B_{12}$	17, 18, 19	52 to 57	2.5×10^{-10}	2.2	0.5
$Zr_{41.2}Ti_{13.8}Cu_{12.5}Ni_{10}Be_{22.5}$	this study	~7000	1.6×10^{-11}	2.7	1 to 3
			1.7×10^{-13}	4.9	
			6.3×10^{-12}	3.4	

of ΔK_{TH} in the metallic glass ranged from ~1 to 3 MPa$\sqrt{\text{m}}$, again comparable to many high-strength steel and aluminum alloys. These data are compared in Table III to results from the only other known fatigue-crack propagation measurements in metallic glass, all of which were performed on rapidly quenched, thin ribbons.[9,11,15–19]

Several points should be noted here. First, whereas in fatigue, growth rates (at 25 Hz and $R = 0.1$) approach catastrophic failure at $\Delta K \sim 12$ MPa$\sqrt{\text{m}}$ ($K \sim 600$ MPa$\sqrt{\text{m}}$ s^{-1} at instability), under monotonic loading, fracture toughnesses as high as ~68 MPa$\sqrt{\text{m}}$ ($K \sim 0.012$ MPa$\sqrt{\text{m}}$ s^{-1}) are measured (Figure 6). Preliminary experimental work suggests that fracture toughness may depend strongly on the loading rate. In Figure 11, for example, fracture toughness is plotted in terms of loading rate for both 7- and 4-mm-thick specimens. Also included on this plot are the points of criticality as measured during fatigue tests at 25 Hz. While there may be a trend toward lower toughness with a higher loading rate, scatter in the data make any conclusions difficult. Second, significant scatter was observed in the crack-growth data from specimen to specimen in the 7-mm-thick samples. This is believed to be associated with the presence of compressive residual stresses in the surface layers of the heats.

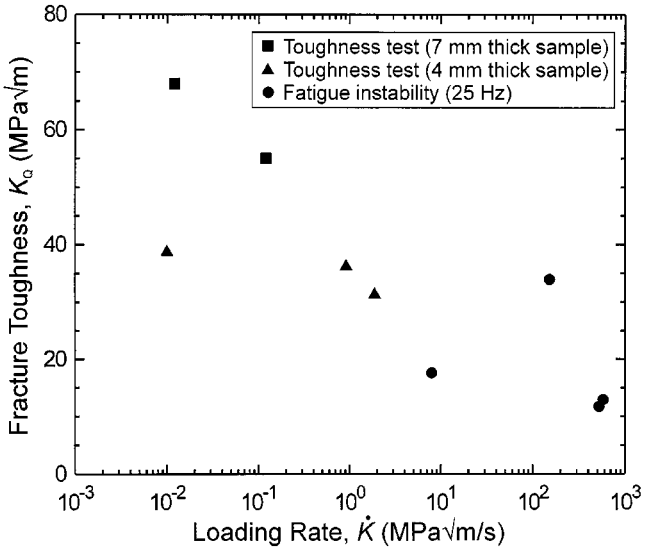

Fig. 11—Variation in the measured fracture toughness, K_Q, of the fully amorphous alloy from both toughness tests and the instability in fatigue-crack propagation tests, as a function of the loading rate, $\dot{K}$.

As the load ratio was increased to $R = 0.5$, cyclic crack growth rates were accelerated and fatigue thresholds were reduced, similar to trends observed in ductile crystalline metals at near-threshold growth rates (Figure 12) and to a rapidly quenched $Ni_{78}Si_{10}B_{12}$ glass alloy (57-μm thick).[19] These data can be expressed in terms of a modified Paris power-law relationship, which includes the effect of both ΔK and K_{max}:[48]

$$\frac{da}{dN} = C(K_{max})^n(\Delta K)^p \qquad [4]$$

where n and p are experimentally determined crack-growth exponents and C is a scaling constant independent of K_{max}, ΔK, and R. In this form, $m = n + p$ and $C = C'(1 - R)^n$ A regression fit of Eq. [4] to the data in Figure 12 yields values of $C = 4.1 \times 10^{-12}$, $n = 2.3$, and $p = 1.2$ (units: m/cycle, MPa$\sqrt{\text{m}}$).

The effect of load-ratio changes on fatigue-crack propagation in crystalline metals (at intermediate-to-low growth

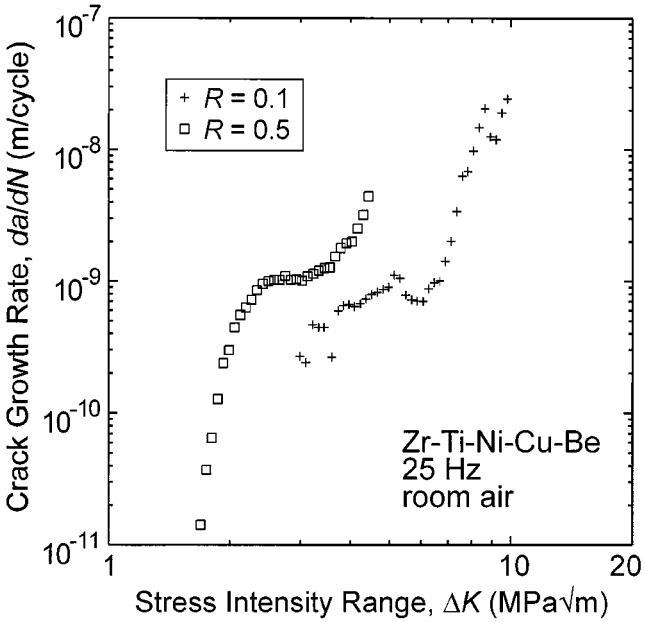

Fig. 12—Results in the form of growth rates, da/dN, plotted as a function of ΔK are shown in the fully amorphous structure for load ratios of $R = 0.1$ and 0.5 ($\nu = 25$ Hz). As the load ratio was increased to $R = 0.5$, cyclic crack growth rates are accelerated and fatigue thresholds, ΔK_{TH}, reduced, similar to behavior in ductile crystalline metals at near-threshold growth rates.

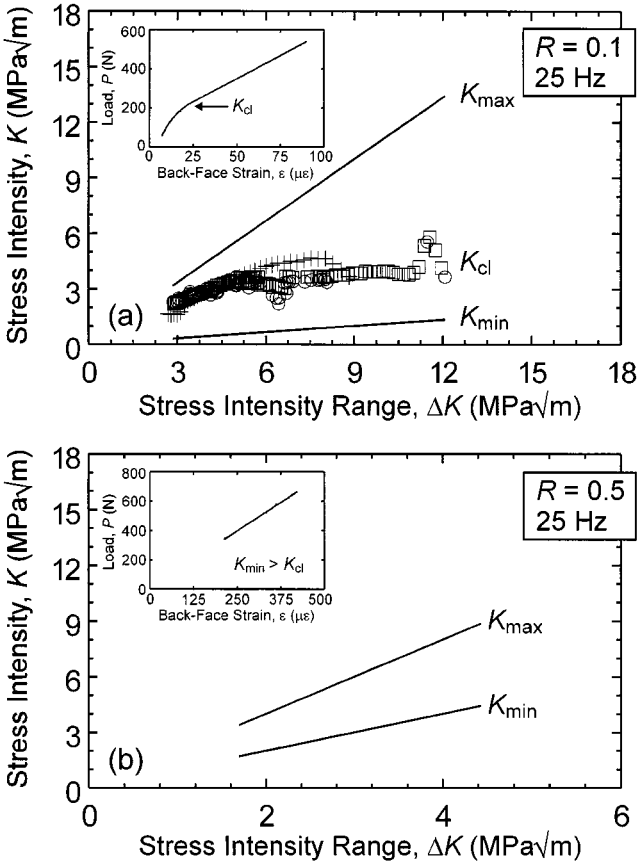

Fig. 13—The stress intensity at crack closure, K_{cl}, was monitored throughout fatigue-crack growth experiments. Whereas significant levels of crack closure were observed at (*a*) $R = 0.1$, such closure was not detected at (*b*) $R = 0.5$. This is shown by the disappearance of nonlinearities in the unloading elastic compliance curves at high R, *i.e.*, insets in (a) and (b).

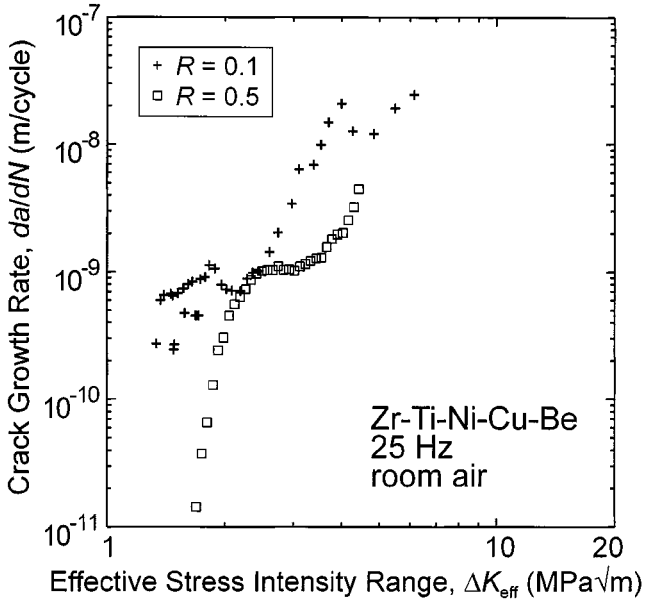

Fig. 14—To account for crack closure, the crack-growth data in Fig. 12 are replotted in terms of the effective stress intensity range, $\Delta K_{eff} = K_{max} - K_{cl}$, where $K_{cl} > K_{min}$.

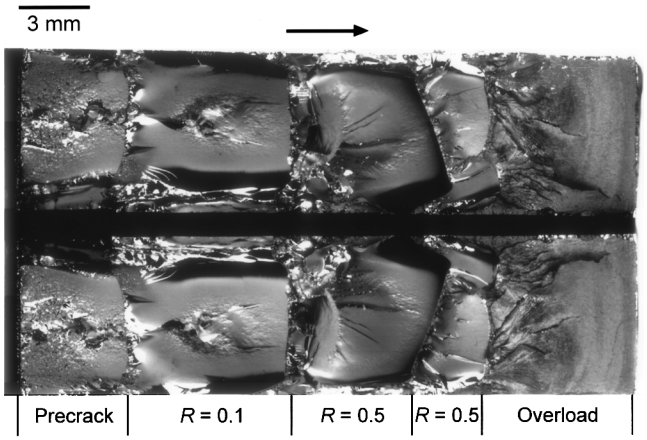

Fig. 15—Opposing fracture surfaces of a compact tension specimen of the fully amorphous alloy subjected to both fatigue and overload fracture. The five visible regions correspond to the initial precrack, one decreasing-ΔK segment at $R = 0.1$, two decreasing-ΔK segments at $R = 0.5$, and finally overload fracture. The arrow indicates the direction of crack propagation.

rates below $\sim 10^{-6}$ m/cycle) is generally associated with crack closure.[49,50,51] Whereas significant levels of crack closure were observed at $R = 0.1$ (Figure 13(a)), no closure was detected at $R = 0.5$ (Figure 13(b)). This is shown by the disappearance of nonlinearities in the unloading elastic compliance curves (compare the insets in Figures 13(a) and 13(b)), as seen on three separate specimens. Using a normalization common to polycrystalline metals, the crack-growth data in Figure 12 were replotted in terms of $\Delta K_{eff} = K_{max} - K_{cl}$, where $K_{cl} > K_{min}$ (Figure 14). Such a normalization is justified by considering that the stress intensity *range* is the primary driving force for fatigue-crack extension in ductile crystalline metals. By ignoring the portion of the loading cycle below K_{cl}, a more appropriate measure of the local crack-tip driving force is obtained, and load-ratio effects can be rationalized.[49,50,51] This normalization is only partially successful when applied to the amorphous alloy (Figure 14).

A macroscopic view of the opposing fracture surfaces of a failed C(T) specimen (~7-mm thick) is shown in Figure 15. The five regions clearly visible on this specimen correspond to various crack-growth experiments, namely, the initial precrack, one decreasing-ΔK segment at $R = 0.1$, two decreasing-ΔK segments at $R = 0.5$, and, finally, overload fracture. The crack front can be seen to propagate evenly through the specimen, with some crack bowing near the edges (likely associated with residual stresses). Such bowing is averaged by the compliance technique used to monitor crack length. The SEM examination of these fatigue surfaces reveals features quite distinct from the vein patterns observed during overload fracture. In general, the roughness of the fracture surfaces scaled directly with local crack-growth rates, with near-threshold regions ($da/dN \sim 10^{-10}$ m/cycle) in many cases exhibiting a mirrorlike surface finish. This mirrorlike appearance is unlike anything observed in more typical polycrystalline metals. In Figure 16(a), the boundary between such a region (on the left) and overload fracture is shown. The surface is relatively featureless, even at higher magnification (Figure 16(b)). Closer examination of the fatigue surfaces showed apparent fatigue striations at both low (Figure 17(a)) and high (Figure 17(b)) driving forces. Although not uniformly covering the fracture surface, the

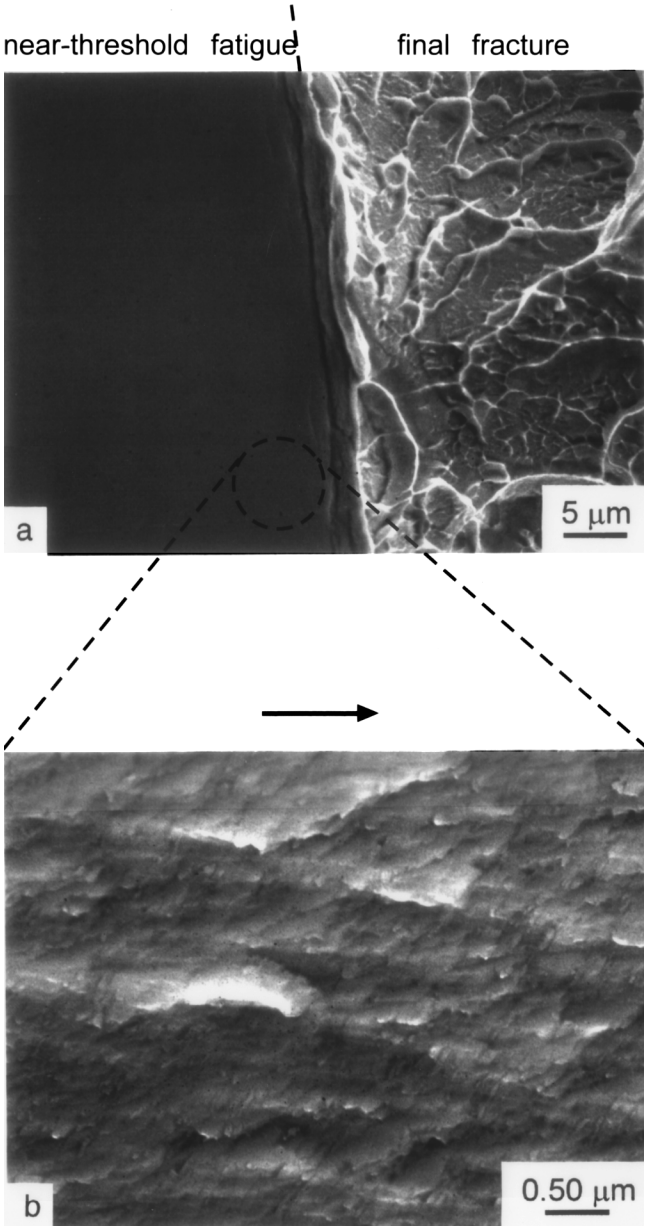

Fig. 16—(*a*) Scanning electron micrograph of the boundary between near-threshold fatigue (on the left) and final fracture (on the right). The near-threshold fatigue region (at $\Delta K < 3$ Mpa$\sqrt{\text{m}}$) has a macroscopic mirrorlike appearance and is nearly featureless, even at higher magnification in (b). The arrow indicates direction of crack propagation.

striation spacing scales with growth rates, as plotted in Figure 10. Moreover, consistent with measurements in rapidly quenched Ni-Fe-[19] and Ni-Si-B-[18] based metallic glasses, the striation spacings significantly overestimate the macroscopic growth rates. Such overestimation is typical of metallic materials at growth rates below $\sim 10^{-6}$ m/cycle and is associated with nonuniform crack extension along the crack front.

Optical microscopic and SEM analysis of crack profiles revealed that fatigue cracks did not generally propagate continuously in the 7-mm-thick specimens. Substantial crack deflection and branching were observed (Figure 18). Flaws frequently nucleated ahead of the main crack, creating large regions of material that spanned the crack faces, resulting

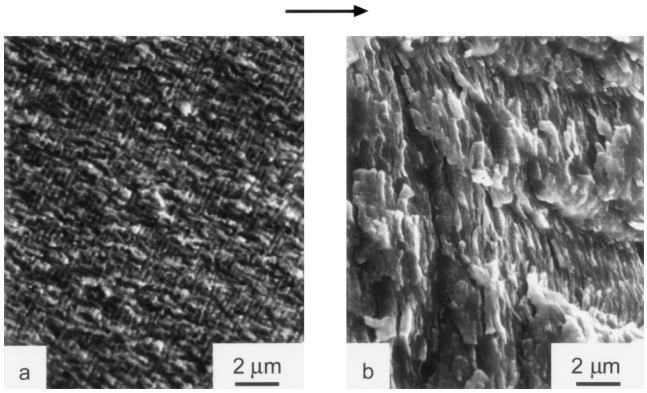

Fig. 17—Scanning electron micrographs of fatigue fracture surfaces in the fully amorphous alloy grown at $R = 0.1$, $\nu = 25$ Hz. In (*a*), $\Delta K \sim 3$ MPa$\sqrt{\text{m}}$ and $da/dN \sim 10^{-10}$ m/cycle, whereas in (*b*), $\Delta K \sim 10$ MPa$\sqrt{\text{m}}$ and $da/dN \sim 10^{-8}$ m/cycle. The arrow indicates the direction of crack propagation.

in a source of crack bridging (Figure 18) and, in some cases, multiple crack branches. The large degree of slip-band formation, which has been observed ahead of fatigue cracks in thin sheets of rapidly quenched amorphous metals,[15,18] was not observed in the present alloy, presumably because deformation was constrained under plane-strain conditions. It is significant to note that, as in polycrystalline metallic alloys, the source of crack closure appeared to be these tortuous, branching crack paths and the rough fracture morphologies (Figure 18). When the minimum stress intensity exceeded K_{cl} at higher load ratios, however, such closure was not observed (Figure 13(b)). Note that such branching, as mentioned previously, was not observed in the 4-mm-thick samples, where the surface layers (and accompanying residual stresses) were machined off.

B. *Variable-Amplitude Fatigue-Crack Growth Behavior*

Results of the variable-amplitude fatigue experiments, specifically involving low-high block overload sequences, are shown in Figure 19(a) for an abrupt transition in ΔK from $\sim$3.2 MPa$\sqrt{\text{m}}$ (near threshold) to $\sim$5.5 MPa$\sqrt{\text{m}}$ ($R = 0.1$, $\nu = 25$ Hz). Immediately after the increase in ΔK, the growth rate markedly increased and then gradually decayed to a new steady-state value. A steady state was reached after $\sim$1 mm of crack extension at a growth rate some two orders of magnitude less than the initial transient (Figure 19(a)). The SEM examination of the fracture surface indicated a distinct change in surface appearance associated with this transient (Figure 19(b)). The almost featureless near-threshold fatigue region (where $da/dN \sim 10^{-10}$ m/cycle) precedes a sharp transition to a rougher surface associated with the higher transient growth rates ($\sim 10^{-7}$ m/cycle). The growth-rate behavior is similar to transients observed in ductile crystalline alloys following block overloads[52] and is similar to behavior measured in a rapidly quenched, thin sheet ($\sim$30 μm thickness) of a Co-Fe-Mo-B-Si metallic glass.[16]

C. *S/N Behavior*

The normalized stress amplitude (σ_a/σ_u) is plotted against cycles to failure in Figure 20(a). Results for the $Zr_{41.2}Ti_{13.8}Cu_{12.5}Ni_{10}Be_{22.5}$ alloy are again compared to those for the

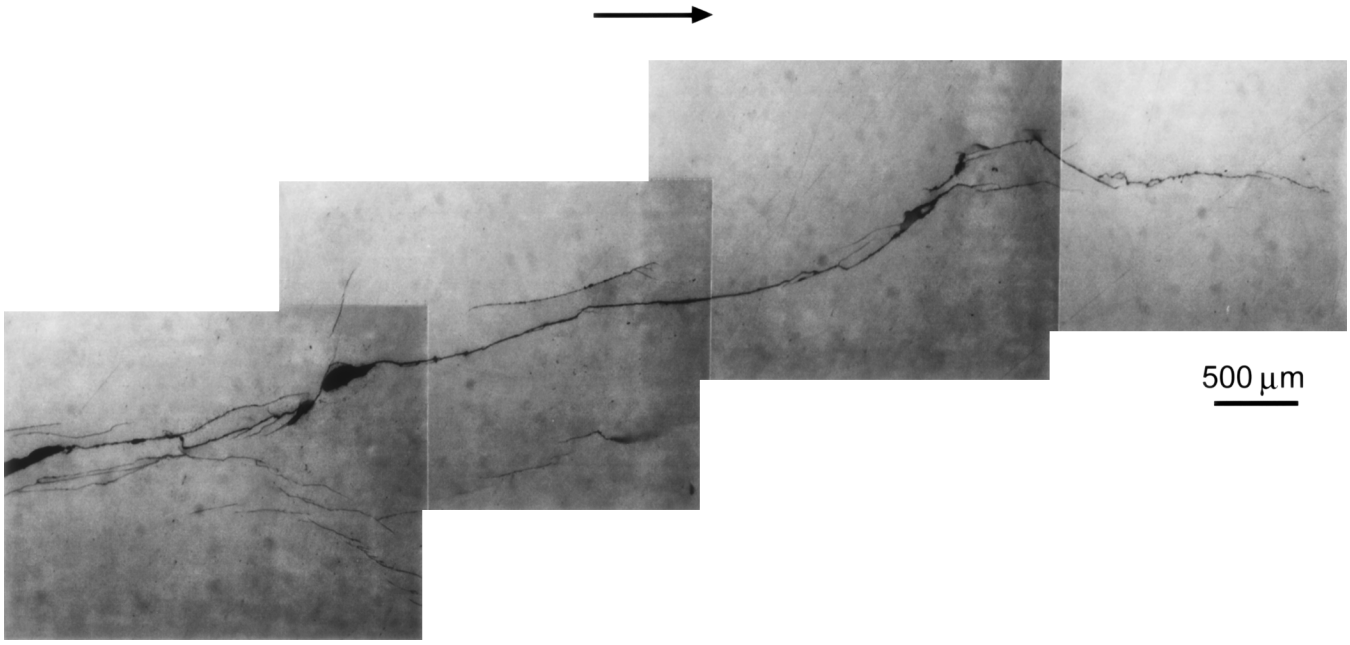

Fig. 18—Optical micrograph of a crack profile grown under cyclic loading ($R = 0.5$, $\nu = 25$ Hz) revealing substantial crack deflection and branching. The arrow indicates the direction of crack growth.

300-M ultrahigh-strength steel (with a comparable tensile strength of 2.3 GPa)[53] and the 2090-T81 aluminum-lithium alloy ($\sigma_u = 0.56$ GPa).[54] It is clear from the comparative plot that the S/N properties of bulk amorphous and polycrystalline metals are very different, despite similarities in crack-growth properties (Figure 10). At a given value of σ_a/σ_u, fatigue lifetimes were significantly shorter in the metallic glass, and lifetimes exhibited a markedly lower dependence on the stress amplitude. For example, by fitting the S/N data to the simple Basquin equation $(\sigma_a)^k N_f = \text{constant}$, fatigue lives in the metallic glass were proportional to $(\sigma_a)^{-3.4}$, compared to $(\sigma_a)^{-10}$ in steel and aluminum. Moreover, whereas steel and aluminum alloys generally display a fatigue limit or 10^7-cycle endurance strength at values of σ_a/σ_u between 0.3 and 0.5 (for $R = 0.1$), no fatigue limit was detected in the metallic glass until σ_a/σ_u dropped below ~0.04. These results are consistent with studies on rapidly quenched thin ribbons of metallic glass, which also indicated a low dependence of fatigue life on the applied-stress amplitude and characteristically lower endurance limits.[10,14,18]

Optical microscopic examination of fatigue fracture surfaces indicated that cracking originated from a corner of the beam at the tensile face of the specimen, with the extent of stable fatigue-crack propagation increasing with life. Beams subjected to high bending stresses (one quarter of a loading cycle) exhibited extensive slip-band formation at the specimen edges, suggesting that slip bands preceded cracking during the S/N experiments. Figure 20(b) shows two such intersecting slip bands. Slip steps are visible at the edge of the specimen (upper left corner) and at the intersection of the two bands (in the center of the micrograph). The band running from the lower left to the upper right formed first, and a jog was created when the other band developed.

At long lives above $N_f \sim 10^6$ cycles (coincident with near-threshold growth rates), the fatigue fracture surfaces consisted primarily of large regions that had a macroscopic mirrorlike appearance. Indeed, the roughness of fatigue surfaces in this alloy was found to diminish progressively with decreasing crack-growth rates, leading to a mirrorlike morphology at near-threshold levels (*i.e.*, at $da/dN \sim 10^{-10}$ m/cycle).[24] The origin of this morphology is unknown, but may involve extensive crack-surface interference between the mating crack surfaces. Detailed SEM analysis of the fracture surfaces indicated a very distinct transition from stable fatigue-crack propagation to overload fracture. For example, the montage in Figure 21 (representing an area $\sim 70 \times 110\ \mu$m) indicates striation-type growth in the fatigue region on the left-hand side, followed by an abrupt change to the vein morphology characteristic of overload fracture in metallic glasses (Figure 8(a)).

V. DISCUSSION

A. *Mechanisms Controlling Fracture in Bulk Metallic Glass*

In brittle solids, fracture or cleavage is initiated when the cohesive strength of the solid is reached at the tip of a pre-existing sharp crack, prior to the onset of extensive inelasticity. Such behavior is generally observed in ceramics and oxide glasses at low homologous temperatures. In crystalline ductile solids, fracture events are dominated by crack-tip plasticity. Progressive separation proceeds by the linkage of voids initiated *via* internal cleavage within brittle particles or by interfacial decohesion at microstructural inhomogeneities.

In contrast to these other classes of materials, the micromechanisms that control tensile fracture and toughness properties of amorphous metals are poorly understood. The fundamental differences in both atomic structure and observed deformation behavior (*e.g.*, extreme slip instability in tension, near-theoretical strength, and distinctive overload

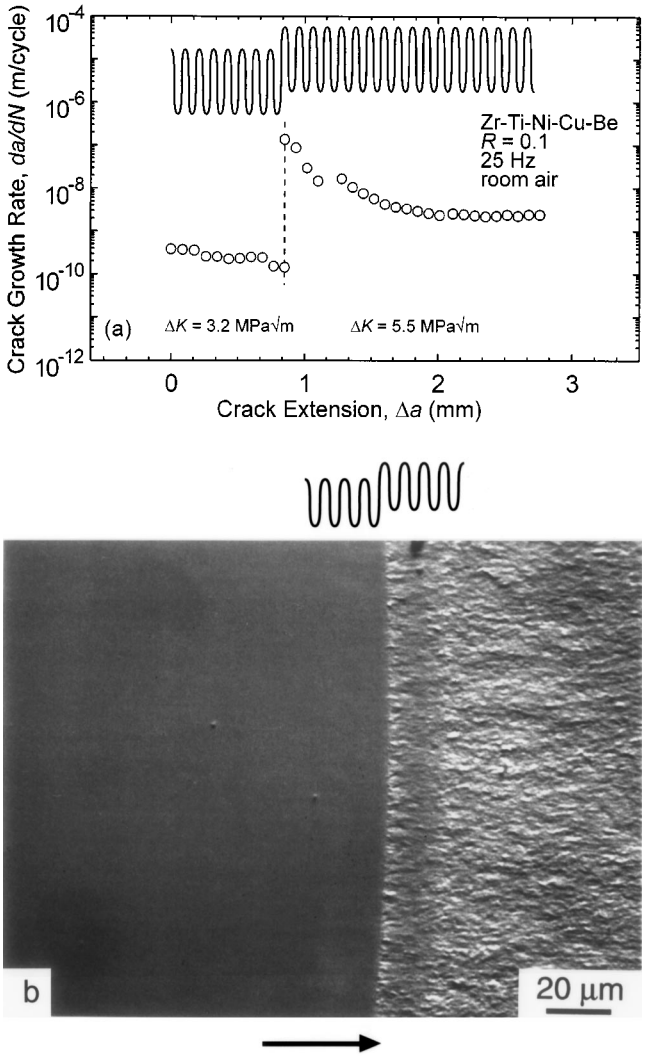

Fig. 19—(*a*) Results for a low-high block overload sequence are shown for an abrupt transition in ΔK from ~3.2 to ~5.5 MPa$\sqrt{m}$ ($R = 0.1$, v = 25 Hz) in the metallic glass. (*b*) A scanning electron micrograph of the fracture surface in this region indicates a distinct change in contrast associated with this overload. The arrow indicates the direction of crack propagation.

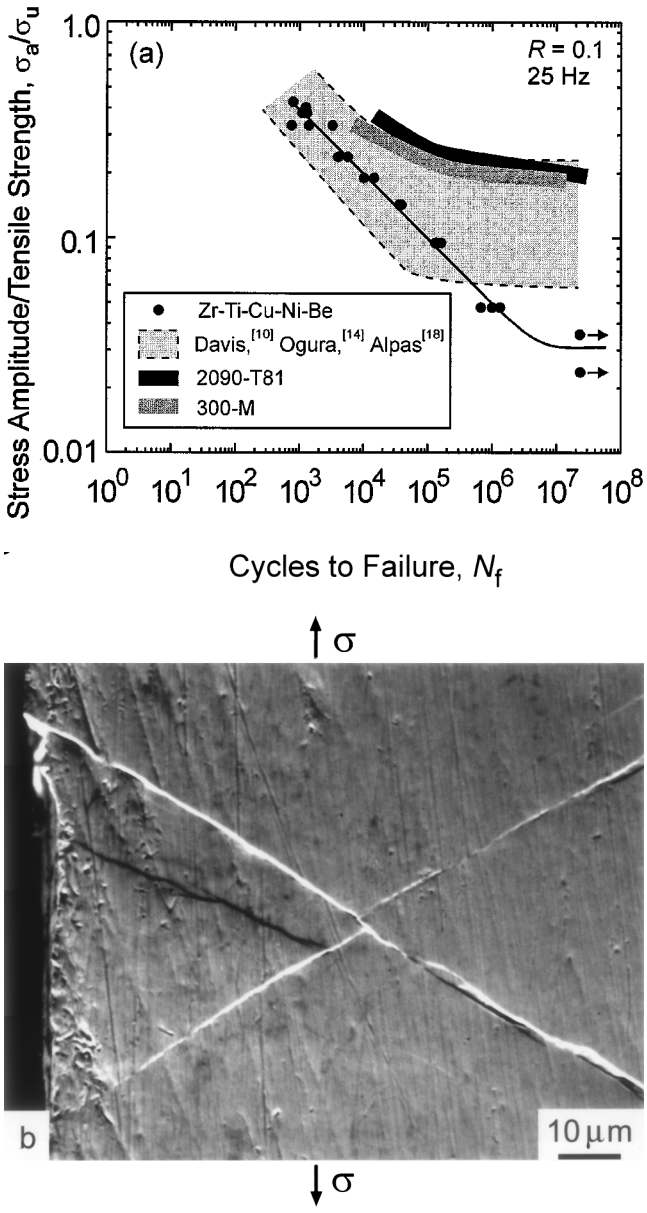

Fig. 20—(*a*) S/N data as the stress amplitude, $\sigma_a = 1/2\ (\sigma_{max} - \sigma_{min})$, normalized by the tensile strength, σ_u, plotted as a function of the number of cycles to failure, N_f, for the bulk metallic glass. Data are compared to high-strength steel (300-M) and aluminum (2090-T81) alloys. (*b*) A scanning electron micrograph showing evidence of slip-band formation at the edge of an S/N specimen.

fracture surface morphologies) make it clear that such mechanisms are quite distinct from tensile fracture in crystalline metals, ceramics, or oxide glasses. Indeed, largely due to the vein morphology (Figures 8(a) through (c)) commonly observed on failure surfaces in metallic glasses,[3,5] some have suggested that fracture in these materials is a variant of the Taylor instability.[3,42] Well studied in the fluids and adhesives literature, this instability is associated with the tendency of a fluid meniscus (under a positive pressure gradient), propagating in the direction of its convex curvature, to break up into a series of fingers which penetrate the fluid meniscus. The process is considered to generate the ubiquitous vein morphology as the material between the fingers necks down to failure. The vein markings are comparable to those observed during the separation of oil or grease films[55] and adhesive films[56] and to those associated with intergranular fracture by diffusional flow at high homologous temperatures in some metals[56] and ceramics.[57] When this process dominates, the critical fracture event is associated with the onset of this instability, governed by the surface tension of the fluid and the applied pressure gradient. The notion that material local to the crack tip is softened, possibly due to adiabatic heating[5,58] or a strain-softening phenomenon,[6,42] is supported by the fracture-surface appearance (Figure 9). In addition, recent measurements have detected significant temperature elevations during deformation[58] and fracture.[59]

Argon and Salama[42] developed a model for the fracture toughness of metallic glasses based on the resistance of a blunt crack to this instability. By determining the critical crack-tip opening displacement (δ) at the onset of the instability, they develop an expression for the fracture toughness:

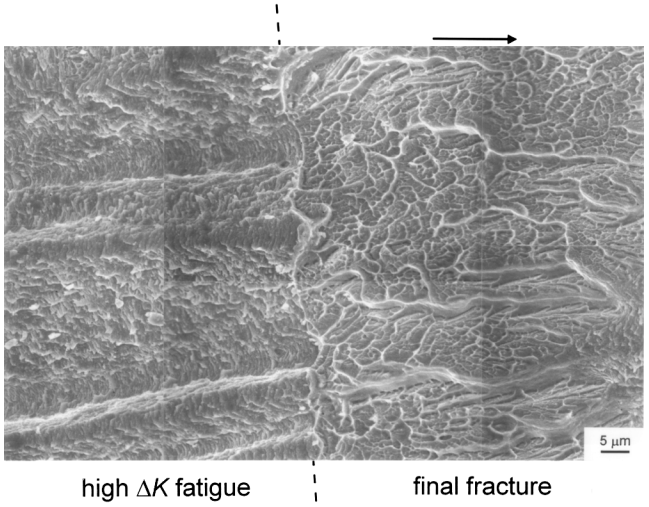

Fig. 21—Scanning electron micrograph of the boundary between fatigue and final fracture on the surface of an S/N beam broken under cyclic loads ($N_f \sim 1.3 \times 10^6$ cycles, σ_a, = 90 MPa). The arrow represents the nominal direction of crack propagation, and the dotted line marks the boundary between fatigue and overload fracture.

$$K_{Ic} = 24\pi^3 \sqrt{3}\,\frac{\beta\Gamma E}{\alpha} \qquad [5]$$

where Γ is the surface tension, β is a scaling constant which depends on the work-hardening behavior, and $\alpha \sim 2.7$.[42] For a solid with near-ideal plastic behavior such as the present alloy, $\beta \sim 4$.[42] Using values of 95 GPa for the modulus (E) and 1 J/m^2 for the surface tension (the surface tensions of the component metals range from ~1 to 2 J/m^2),[60] Eq. [5] predicts a K_{Ic} value of merely ~13 MPa$\sqrt{\text{m}}$, far lower than our measured values. It is speculated that the discrepancy between measured and calculated toughness may be associated with a strain-rate effect or with extensive crack branching and ligament bridging observed along the fatigue crack prior to the measurement of toughness (*e.g.*, Figure 18). Such mechanisms are known to be quite potent in promoting toughness[61] and are obviously not accounted for in Eq. [5]. In fact, Lowhaphandu *et al.*[28] observed no crack branching and measured a fracture toughness of 18.4 ± 1.4 MPa$\sqrt{\text{m}}$.

The severe embrittlement observed upon full crystallization is presumed to be associated with the complex intermetallic crystal structure that forms (five separate solid solutions in equilibrium in the present alloy).[33–35,37] However, it is surprising that the toughness plummets with the precipitation of as little as 5 vol pct nanocrystals in an otherwise amorphous matrix (after annealing at 633 K for 12 hours). At 5 vol pct, such nanocrystals cannot yet form a continuous network. The severe embrittlement must, therefore, also involve changes in the remaining amorphous material (such as the local concentration of certain elements). At this point, however, no specific mechanisms are known for fracture in the semicrystalline microstructures.

B. *Mechanisms for Fatigue Degradation in Bulk Metallic Glass*

1. *Crack propagation*

The mechanism of striation formation in crystalline alloys is associated with irreversible crack-tip shear that alternately blunts and resharpens the crack during the fatigue cycle. Models for striation formation[62] indicate that growth rates should scale with the range of crack-tip opening displacement ($\Delta\delta$). Using simple continuum-mechanics arguments,[62]

$$\frac{da}{dN} \propto \Delta\delta \sim \beta' \frac{\Delta K^2}{\sigma_Y E'} \qquad [6]$$

where σ_Y is the flow stress, $E' = E$ in plane stress or $E/(1 - \nu^2)$ in plane strain, and β' is a scaling constant (~0.01 to 0.1 for mode I crack growth) which is a function of the degree of slip reversibility and elastic-plastic properties of the material. In amorphous metals, tensile experiments indicate that slip bands also form readily[2,30] (Figure 20(b)). Moreover, Eq. [6] provides a reasonable description of the experimentally measured growth rates with $\beta' \sim 0.01$ (Figure 10). Together with the presence of fatigue striations on the fracture surfaces (Figure 17), this suggests a mechanism for cyclic crack advance in metallic glasses which also involves repetitive blunting and resharpening of the crack tip.

2. *Variable-amplitude fatigue-crack growth behavior*

Following an abrupt change in ΔK, crack-growth transients are commonly observed in polycrystalline metals.[46] In these materials, orders of magnitude of retardation in growth rates (and even arrest) are observed following single tensile overloads or high-low block-loading sequences, whereas transient accelerations generally follow low-high sequences. In both cases, the extent of crack growth affected is comparable to the size of the overload plastic (or transformation) zone created ahead of the crack tip.[52] In polycrystalline metals, the transients are associated with a variety of mechanisms, including crack deflection and the generation of residual stresses in the overload plastic zone, and the subsequent enhanced effect of crack closure in the wake of the crack tip. The fact that significant crack-growth transients are observed in $Zr_{41.2}Ti_{13.8}Cu_{12.5}Ni_{10}Be_{22.5}$ amorphous metal suggests that similar mechanisms may be operating here.

3. *Crack initiation*

The results in Figures 10 and 20(a) present an interesting contrast between crystalline and amorphous metals. Whereas the crack-propagation properties (Figure 10) are similar in the two classes of materials (with respect to the presence of fatigue striations and the dependence of growth rates on ΔK), the S/N behavior (Figure 20(a)) is markedly different. In the S/N measurements, total life is far less dependent upon the applied stress amplitude, and the fatigue limit is smaller by one order of magnitude. This implies that, mechanistically, the fatigue properties of crystalline and amorphous metals differ significantly with respect to crack *initiation*, or, more precisely, in the nucleation of crack growth. Such a difference may be associated with the easier natural initiation of a fatigue crack, *e.g.*, *via* slip-band formation (Figure 20(b)),[30] although very little is known about the initiation mechanisms at this time. However, since the fatigue limit can be equated with the critical stress for crack initiation or, more generally, for an initiated (small) crack to overcome some microstructural barrier (*e.g.*, a grain boundary),[63] we may presume that the markedly lower fatigue limits in the amorphous alloys are associated with a lack of microstructure, which would normally provide local arrest points to newly initiated or preexisting cracks. Indeed, low endurance limits appear to be typical of metallic glass.[10,14,18] Recent work on the development of bulk metallic-glass matrix composites, however, may

be useful in mitigating this problem by introducing crack-arresting barriers back into the microstructure.[64,65]

VI. SUMMARY AND CONCLUSIONS

1. Significant variability was observed in measured fracture toughness for the fully amorphous $Zr_{41.2}Ti_{13.8}Cu_{12.5}Ni_{10}Be_{22.5}$ alloy. Sources of this variability are likely associated with residual stresses at the surface of castings, compositional variation (particularly oxygen), crack branching and ligament bridging, and sensitivity to loading rate. The latter is suggested by a large discrepancy between criticality, as measured during fatigue tests and during fracture toughness tests.

2. In the partially or fully crystallized condition, the alloy displays a marginal increase in hardness and a severe drop in fracture toughness. As shown *via* depth-sensing indentation experiments and fracture-surface examination, the embrittlement was accompanied by a distinct change in the deformation mode.

3. Preliminary attempts to rationalize the fracture toughness of the amorphous structure indicate that a model based on the Taylor instability underpredicts the measured K_Q values. The higher measured toughness is considered to result from strain-rate effects and/or extensive branching, deflection, and bridging of the crack associated with surface residual stress.

4. The amorphous $Zr_{41.2}Ti_{13.8}Cu_{12.5}Ni_{10}Be_{22.5}$ alloy is susceptible to fatigue degradation. Crack-growth behavior is similar to that observed in traditional ductile crystalline alloys in terms of (a) the dependence of growth rates on the applied stress-intensity range, (b) the role of load ratio and crack closure, and (c) the presence of ductile striations on fatigue fracture surfaces.

5. Conversely, the S/N behavior of the metallic glass was very different from that observed in ductile crystalline alloys. Fatigue lifetimes were shorter in the amorphous alloy and exhibited a far lower dependence on the applied stress range. A fatigue limit could not be detected until the stress amplitude dropped to ~4 pct of the tensile strength. This difference is likely associated with the lack of microstructural barriers to the growth of pre-existing or newly initiated cracks.

ACKNOWLEDGMENTS

This work was supported by the United States Air Force Office of Scientific Research under Grant No. F49620-98-1-0260. Thanks are also due to Drs. A. Peker and M. Tenhover, Amorphous Technologies International, Corp., for their support and for supplying the material, and to Howmet Research Corp. for additional financial support. The authors also thank Professor W.L. Johnson, California Institute of Technology, for microscopy and numerous helpful discussions, and Professor R. Pippan and Mr. A. Tatschl, Erich-Schmid-Institut fur Festorperphysik (Leoben, Austria) for stereophotogrammetric measurements of fracture surfaces.

REFERENCES

1. W. Klement, R.H. Willens, and P. Duwez: *Nature*, 1960, vol. 187, pp. 869-70.
2. J.J. Gilman: *J. Appl. Phys.*, 1975, vol. 46, pp. 1625-33.
3. C.A. Pampillo and A.C. Reimschuessel: *J. Mater. Sci.*, 1974, vol. 9, pp. 718-24.
4. A.S. Argon: *Acta Metall.*, 1979, vol. 27, pp. 47-58.
5. H.J. Leamy, H.S. Chen, and T.T. Wang: *Metall. Trans.*, 1972, vol. 3, pp. 699-708.
6. F. Spaepen: *Acta Metall.*, 1977, vol. 25, pp. 407-15.
7. H. Kimura and T. Masumoto: *Scripta Metall.*, 1975, vol. 9, pp. 211-22.
8. D. Srolovitz, V. Vitek, and T. Egami: *Acta Metall.*, 1983, vol. 31, pp. 335-52.
9. L.A. Davis: *J. Mater. Sci.*, 1975, vol. 10, pp. 1557-64.
10. L.A.Davis: *J. Mater. Sci.*, 1976, vol. 11, pp. 711-17.
11. D.G. Ast and D. Krenitsky: *Mater. Sci. Eng.*, 1976, vol. 23, pp. 241-46.
12. S. Takayama and R. Maddin: *Mater. Sci. Eng.*, 1976, vol. 23, pp. 261-65.
13. L.A. Davis: *Metall. Trans. A*, 1979, vol. 10A, pp. 235-40.
14. T. Ogura, T. Masumoto, and K. Fukushima: *Scripta Metall.*, 1975, vol. 9, pp. 109-14.
15. T. Ogura, K. Fukushima, and T. Masumoto: *Mater. Sci. Eng.*, 1976, vol. 23, pp. 231-35.
16. T.K. Chaki and J.C.M. Li: *Scripta Metall.*, 1984, vol. 18, pp. 703-08.
17. A.T. Alpas, L. Edwards, and C.N. Reid: *Mater. Sci. Eng.*, 1988, vol. 98, pp. 501-04.
18. A.T. Alpas, L. Edwards, and C.N. Reid: *Metall. Trans. A*, 1989, vol. 20A, pp. 1395-1409.
19. A.T. Alpas, L. Edwards, and C.N. Reid: *Eng. Fract. Mech.*, 1990, vol. 36, pp. 77-92.
20. A. Inoue, T. Nakamura, N. Nishiyama, and T. Masumoto: *Mater. Trans., JIM*, 1992, vol. 33, pp. 937-45.
21. A. Inoue, T. Zhang, and A. Takeuchi: *Appl. Phys. Lett.*, 1997, vol. 71, pp. 464-66.
22. A. Peker and W.L. Johnson: *Appl. Phys. Lett.*, 1993, vol. 63, pp. 2342-44.
23. X.H. Lin and W.L. Johnson: *J. Appl. Phys.*, 1995, vol. 78, pp. 6514-19.
24. C.J. Gilbert, R.O. Ritchie, and W.L. Johnson: *Appl. Phys. Lett.*, 1997, vol. 71, pp. 476-78.
25. C.J. Gilbert, J.M. Lippmann, and R.O. Ritchie: *Scripta Mater.*, 1998, vol. 38, pp. 537-42.
26. R.D. Conner, A.J. Rosakis, W.L. Johnson, and D.M. Owen: *Scripta Mater.*, 1997, vol. 37, pp. 1373-78.
27. C.T. Liu, L. Heatherly, D.S. Easton, C.A. Carmichael, J.H. Schniebel, C.H. Chen, J.L. Wright, M.H. Yoo, J.A. Horton, and A. Inoue: *Metall. Mater. Trans. A*, 1998, vol. 29A, pp. 1811-20.
28. P. Lowhaphandu and J.J. Lewandowski: *Scripta Mater.*, 1998, vol. 38, pp. 1811-17.
29. M. Calvo-Dahlborg: *Mater. Sci. Eng.*, 1997, vols. A226–A228, pp. 833-45.
30. H.A. Bruck, T. Christman, A.J. Rosakis, and W.L. Johnson: *Scripta Metall. Mater.*, 1994, vol. 30, pp. 429-34.
31. W.L. Johnson and A. Peker: in *Science and Technology of Rapid Solidification and Technology*, M.A. Otooni, ed., Kluwer Academic Publishers, Dordrecht, The Netherlands, 1995, pp. 25-41.
32. W.L. Johnson: California Institute of Technology, Pasadena, CA, unpublished research, 1997.
33. R. Busch, S. Schneider, A. Peker, and W.L. Johnson: *Appl. Phys. Lett.*, 1995, vol. 67, pp. 1544-46.
34. S.P. Schneider, P. Thiyagarajan, and W.L. Johnson: *Appl. Phys. Lett.*, 1996, vol. 68, pp. 493-95.
35. A. Peker and W.L. Johnson: *Mater. Sci. Eng.*, 1994, vols. A179–A180, pp. 173-75.
36. H.J. Fecht: *Phil. Mag. B*, 1997, vol. 76, pp. 495-503.
37. S. Spriano, C. Antonione, R. Doglione, L. Battezzati, S. Cardoso, J.C. Soares, and M.F. da Silva: *Phil. Mag. B*, 1997, vol. 76, pp. 529-40.
38. I. Finnie and W. Cheng: *J. Eng. Mater. Technol.*, 1995, vol. 117, pp. 373-78.
39. C.J. Gilbert, W. Cheng, V. Schroeder, and R.O. Ritchie: unpublished research, 1999.
40. B.R. Lawn: *Fracture of Brittle Solids*, 2nd ed., Cambridge University Press, Cambridge, United Kingdom, 1993.
41. A. Tatschl and R. Pippan: Austrian Academy of Science, Leoben, Austria, private communication, 1997.
42. A.S. Argon and M. Salama: *Mater. Sci. Eng.*, 1976, vol. 23, pp. 219-30.
43. R.O. Ritchie: *J. Eng. Mater. Technol. Trans. ASME Ser. H*, 1977, vol. 99, pp. 195-204.
44. K.T. Venkateswara Rao, W. Yu, and R.O. Ritchie: *Metall. Trans. A*, 1988, vol. 9A, pp. 549-61.
45. P.C. Paris and F. Erdogan: *J. Basic Eng.*, 1963, vol. 85, pp. 528-34.

46. C.J. Gilbert, R.H. Dauskardt, R.W. Steinbrech, R.N. Petrany, and R.O. Ritchie: *J. Mater. Sci.*, 1995, vol. 30, pp. 643-54.
47. S.J. Dill, S.J. Bennison, and R.H. Dauskardt: *J. Am. Ceram. Soc.*, 1997, vol. 80, pp. 773-76.
48. R.H. Dauskardt, M.R. James, J.R. Porter, and R.O. Ritchie: *J. Am. Ceram. Soc.*, 1992, vol. 75, pp. 759-71.
49. W. Elber: *Eng. Fract. Mech.*, 1970, vol. 2, pp. 37-45.
50. R.A. Schmidt and P.C. Paris: *Progress in Flaw Growth and Fracture Toughness Testing*, ASTM, Philadelphia, PA, 1973, pp. 79-94.
51. S. Suresh and R.O. Ritchie: in *Fatigue Crack Growth Threshold Concepts*, D.L. Davidson and S. Suresh, eds., TMS-AIME, Warrendale, PA, 1984, pp. 227-61.
52. C.M. Ward-Close, A.F. Blom, and R.O. Ritchie: *Eng. Fract. Mech.*, 1989, vol. 32, pp. 613-38.
53. W.F. Brown, Jr.: *Aerospace Structural Metals Handbook*, Metals and Ceramics Information Center, Syracuse, NY, 1989, vol. code 1224, pp. 1-30.
54. K.T. Venkateswara Rao and R.O. Ritchie: *Int. Mater. Rev.*, 1992, vol. 37, pp. 153-85.
55. G.I. Taylor: *Proc. R. Soc. London*, 1950, vol. A201, pp. 192-96.
56. R.J. Fields and M.F. Ashby: *Phil. Mag.*, 1976, vol. 33, pp. 33-48.
57. R.L. Tsai and R. Raj: *Acta Metall.*, 1982, vol. 30, pp. 1043-58.
58. H.A. Bruck, A.J. Rosakis, and W.L. Johnson: *J. Mater. Res.*, 1996, vol. 11, pp. 503-11.
59. C.J. Gilbert, J.W. Ager III, V. Schroeder, J.P. Lloyd, J.R. Graham, and R.O. Ritchie: *Appl. Phys. Lett.*, 1999, in press.
60. M.A. LaMadrid, S.D. O'Connor, A. Peker, W.L. Johnson, and J.D. Baldeschwieler: *J. Mater. Res.*, 1996, vol. 11, pp. 1494-99.
61. R.O. Ritchie: *Mater. Sci. Eng.*, 1988, vol. A103, pp. 15-28.
62. F.A. McClintock and R.M.N. Pelloux: "*Boeing Scientific Research Laboratories Document* D1-82-0708", 1968, cited in R.M.N. Pelloux: *Trans. ASM*, 1969, vol. 62, pp. 281-85.
63. K.J. Miller: *Fat. Fract. Eng. Mater. Struct.*, 1987, vol. 10, pp. 93-113.
64. H. Choi-Yim, R. Busch, and W.L. Johnson: *J. Appl. Phys.*, 1998, vol. 83, pp. 7993-97.
65. R.B. Dandliker, R.D. Conner, and W.L. Johnson: *J. Mater. Res.*, 1998, vol. 13, pp. 2896-2901.